

Accelerating discovery of infrared nonlinear optical materials with large shift current via high-throughput screening

Aiqin Yang¹, Dian Jin^{2,3}, Mingkang Liu^{2,4}, Daye Zheng^{2,*}, Qi Wang^{5,6,*}, Qiangqiang Gu^{2,5,7,8,*}, and Jian-Hua Jiang^{1,5,6,9,*}

¹School of Physical Science and Technology, Soochow University, Suzhou 215006, China

²AI for Science Institute, Beijing 100080, China

³Research Institute for Intelligent Wearable Systems, The Hong Kong Polytechnic University, Hong Kong SAR, China

⁴Department of Mechanical Engineering, National University of Singapore, Singapore 117575, Singapore

⁵Suzhou Institute for Advanced Research, University of Science and Technology of China, Suzhou 215123, China

⁶School of Biomedical Engineering, Division of Life Sciences and Medicine, University of Science and Technology of China, Hefei 230026, China

⁷School of Artificial Intelligence and Data Science, University of Science and Technology of China, Hefei 230026, China

⁸Suzhou Big Data & AI Research and Engineering Center, Suzhou 215123, China

⁹School of Physical Sciences, University of Science and Technology of China, Hefei 230026, China

*zhengdy@aisi.ac.cn

*qiw@ustc.edu.cn

*guqq@ustc.edu.cn

*jhjiang3@ustc.edu.cn

ABSTRACT

Discovering nonlinear optical (NLO) materials with strong shift current response, particularly in the infrared (IR) regime, is essential for next-generation optoelectronics yet remains highly challenging in both experiments and theory, which still largely relies on case by case studies. Here, we employ a high-throughput screening strategy, applying a multi-step filter to the Materials Project database (>154,000 materials), which yielded 2,519 candidate materials for detailed first-principle evaluation. From these calculations, we identify 32 NLO materials with strong shift current response ($\sigma > 100 \mu A/V^2$). Our work reveals that layered structures with C_{3v} symmetry and heavy p -block elements (e.g. Te, Sb) exhibit apparent superiority in enhancing shift current. More importantly, 9 of these compounds show shift current response peaks in the IR region, with the strongest reaching $616 \mu A/V^2$, holding significant application potential in fields such as IR photodetection, sensing, and energy harvesting. Beyond identifying promising candidates, this work establishes a comprehensive and high-quality first-principles dataset for NLO response, providing a solid foundation for future AI-driven screening and accelerated discovery of high-performance NLO materials, as demonstrated by a prototype machine-learning application.

Introduction

The efficient conversion of light into electricity underpins a broad range of technologies, from imaging and communications to biosensing and renewable energy^{1,2}. Beyond the traditional photovoltaic effect (PVE) based on $p-n$ junctions (Fig. 1(a)), whose open-circuit voltage is fundamentally bounded by the material's bandgap³⁻⁶, the bulk photovoltaic effect (BPVE) offers a distinct, interface-free mechanism enabled by inversion-symmetry breaking (Fig. 1(b)). The BPVE occurring in non-centrosymmetric materials, a second-order nonlinear photoelectric response, can generate steady direct-current photocurrent and above-bandgap photovoltages⁷⁻⁹, making them a promising platform for next-generation nonlinear optoelectronics. Microscopically, the photocurrent observed in BPVE is understood as arising from two primary mechanisms: ballistic current and shift current⁹. Ballistic current is a more extrinsic mechanism involving complex scattering processes^{10,11}. In contrast, shift current is widely considered an intrinsic mechanism, largely insensitive to scattering¹²⁻¹⁴. Under uniform illumination, electron excitation from valence to conduction bands in non-centrosymmetric materials produces an asymmetric momentum distribution accompanied

by a shift in real-space positions^{15,16}, resulting in a net shift current along the material's spontaneous polarization direction (Fig. 1(c)). This work focuses specifically on shift current in BPVE.

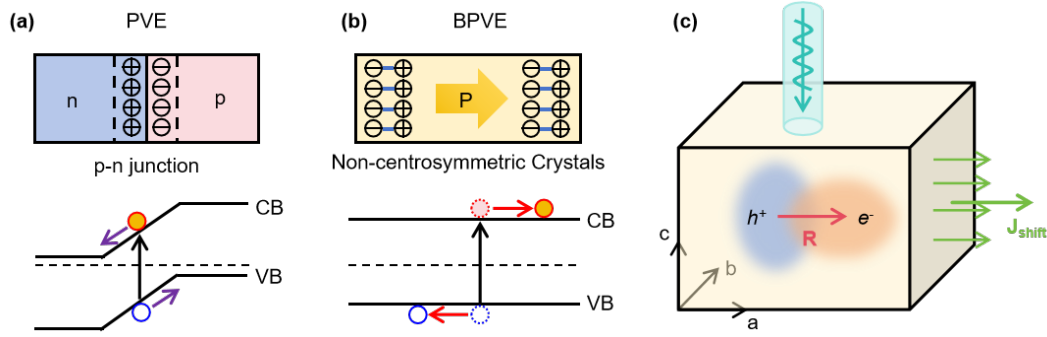


Figure 1. Schematic illustration of traditional photovoltaic effect (PVE) and bulk photovoltaic effect (BPVE). (a) Traditional PVE devices, such as p-n junctions, utilize the built-in electric field near the junction interface to separate photo-excited carriers. (b) BPVE is an intrinsic photovoltaic phenomenon occurring in non-centrosymmetric materials, relying on spontaneous polarization induced by structural asymmetry to separate photo-excited charge carriers without requiring heterojunctions or interfaces. (c) The shift current mechanism in real space on light-induced interband excitation. In non-centrosymmetric crystals, the displacement of the electron cloud during the excitation of electrons from the valence band to the conduction band generates a net current known as shift current.

Early demonstrations of shift current BPVE were reported in ferroelectric oxides, such as BaTiO_3 ^{17,18}, LiNbO_3 ¹⁹, and $\text{Pb}(\text{ZrTi})\text{O}_3$ ²⁰. Due to their wide bandgap (2.7–4 eV), these materials typically exhibit photovoltaic response mainly in the ultraviolet (UV) to visible (VIS) spectrum. The development of emerging materials, such as two-dimensional materials and topological semimetals, has led to more extensive and in-depth studies of BPVE, extending its spectral response range into the IR and even terahertz (THz) regions. Osterhoudt et al.²¹ reported a giant shift current response in Weyl semimetal TaAs ($\sigma^{\text{aac}} \sim 154 \mu\text{A}/\text{V}^2$ at $10.6 \mu\text{m}$) exceeding conventional ferroelectrics by an order of magnitude, pushing the operational wavelength of BPVE deep into the mid-infrared (MIR). Wang et al.²² further demonstrated broadband coverage from UV to MIR (390 nm–3.8 μm) in tellurium, achieving an extraordinary photocurrent density of $70.4 \text{ A}/\text{cm}^2$ at $1.31 \mu\text{m}$. These breakthroughs establish shift current BPVE as a powerful mechanism spanning VIS to THz wavelengths with unprecedented intensity. IR wavelengths constitute a vital segment of the electromagnetic spectrum, characterized by low energy and strong penetration power, playing a significant role across multiple fields including industry, medicine, and military applications. Given that the BPVE generates steady direct-current photocurrent without external voltage and can theoretically surpass the Shockley-Queisser (S-Q) limit of traditional PVE, the IR shift current holds immense potential in high-sensitivity IR detection without external bias, self-powered optoelectronic sensing, broad-spectrum energy harvesting, and deep biomedical regulation. However, the practical application of BPVE remains constrained by low photocurrents and poor energy conversion efficiency. Therefore, identifying materials capable of strong shift current response, particularly within the IR spectrum, represents an urgent and critical research priority.

A comprehensive computational search offers a promising pathway for accelerating discovery of NLO materials with strong shift current response. The high-throughput screening approach has successfully identified high-performance candidates across diverse applications, from photovoltaics²³ and nonlinear optics²⁴ to power electronics²⁵, thermoelectrics²⁶ and field-effect transistors²⁷, far surpassing traditional trial-and-error methods. However, current high-throughput efforts based on BPVE have been limited to either specific structural families, such as the two-dimensional $\text{CuXX}'\text{Y}$ materials²⁸, or small databases, such as the 326 non-centrosymmetric entries in the C2DB²⁹. Critically, no systematic exploration of NLO shift current response has been conducted across the much broader Materials Project (MP) database, which contains more than 154,000 inorganic materials. This leaves the large structural and chemical space of MP essentially uncharted for high-performance IR shift-current materials. Meanwhile, the rapid rise of AI-assisted materials discovery highlights the indispensable role of high-quality, large-scale datasets in the development of predictive and generative models. For NLO effect, particularly the shift current, such datasets are virtually missing, causing a severe bottleneck for advancing data-driven discovery pipelines. Establishing a reliable first-principles dataset for shift-current response is therefore as fundamental as improving the underlying machine-learning models themselves.

In this work, we address these gaps by performing unbiased high-throughput first-principles calculations, with the exchange-correlation functional in the Perdew-BurkeErnzerhof (PBE) form³⁰, on 2,519 non-centrosymmetric materials filtered from the MP database. From these calculations, 32 materials exhibiting strong shift current response ($\sigma > 100 \mu\text{A}/\text{V}^2$) were identified.

For these top 32 candidates, we further performed Heyd-Scuseria-Ernzerhof (HSE) hybrid functional^{31,32} calculations to obtain more accurate bandgaps and NLO response. Ultimately, we identified 9 NLO materials that exhibit pronounced shift current peaks within the IR range as well as 20 and 5 NLO materials with peak response in the VIS and UV ranges, respectively. These infrared candidate materials expand the BPVE material landscape and establish promising platforms for IR-related technologies such as IR sensing, imaging and communications. Finally, beyond identifying promising materials, our high-throughput workflow also generates one of the most comprehensive first-principles datasets of shift-current response to date. A simple machine-learning demonstration based on DPA3- σ model further illustrates its potential for accelerating large-scale, data-driven screening of NLO materials which can find valuable applications in lasing, photo-detection, and quantum information processing for various frequencies. Together, these efforts establish a robust foundation for advancing both physics-based and AI-driven discovery of high-performance IR shift current materials.

Results

Database screening and high-throughput calculations

Our high-throughput screening workflow, illustrated in Fig. 2(a), commences with the 154,879 inorganic compounds in the MP database³³. A multi-step filtering procedure was applied to identify non-centrosymmetric, thermodynamically reasonable, and computationally tractable candidates suitable for shift current calculations. The screening criteria are as follows: (1) Symmetry: materials must be non-centrosymmetric, which yielded 57,682 structures. (2) Electronic structure: candidates were selected to have a PBE band gap $E_g > 0.1$ eV and be non-magnetic. (3) Thermodynamic stability: structures with an energy above the convex hull $E_{\text{hull}} \leq 50$ meV/atom were selected as potentially synthesizable. (4) Elemental composition: systems containing elements with partially filled 3d shells (V, Cr, Mn, Fe, Co, Ni) or lanthanide/actinide elements were removed to avoid uncertainties in density functional theory (DFT) treatment of localized d/f electrons. (5) Computational tractability: structures with fewer than 20 atoms per unit cell were retained to ensure feasible high-throughput calculations. Beyond this restriction, no further bias toward specific chemistries or structure types was imposed.

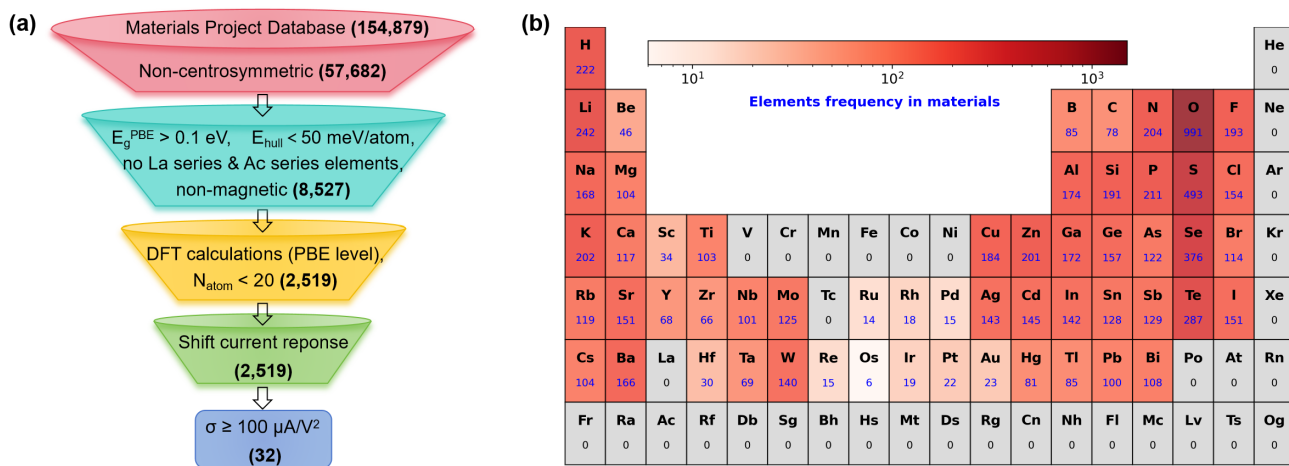


Figure 2. Database screening and high-throughput calculations. (a) The workflow of high-throughput screening process. Initially, filters based on symmetry, band gap, number of atoms, magnetic properties, and elemental composition are applied. Subsequently, DFT calculations are conducted to obtain the Hamiltonian and band structure. Following this, the DFT Hamiltonians are utilized to compute the shift current response at the PBE level. Ultimately, 32 materials with high shift current response are identified as potential candidates. Importantly, further calculations at the HSE level are performed for these target candidates to refine the results. (b) The distribution of 56 elements in the periodic table for 2,519 noncentrosymmetric materials, where the color intensity represents the frequency of occurrence in all screened materials, and the numbers below the chemical symbols show the count of occurrence of that element. Gray represents elements that did not appear in this study.

Following these filtering steps, 2,519 candidate materials remained for first-principles evaluation. For these filtered candidates, we employed a two-stage computational strategy. First, the electronic structure and optical response for all 2,519 candidates were computed using the PBE exchange-correlation functional. Recognizing that the shift current response is highly sensitive to band structure details and that PBE tends to underestimate band gaps, we performed a second stage of calculations. Specifically, we identified the 32 most promising materials (defined in the next section as those with a PBE response $\sigma > 100 \mu\text{A/V}^2$) and performed more accurate HSE hybrid functional³² calculations to obtain refined electronic

structures and NLO response.

Statistical analysis of shift current response preference

Fig. 2(b) illustrates the elemental distribution of the screened 2,519 noncentrosymmetric materials covering 56 elements across the periodic table, with color intensity representing their frequency of occurrence in the screened material and the numbers below the chemical symbols indicating their count. It can be observed that element oxygen appears most frequently (991 occurrences) among the screened materials. Except for elements excluded by the screening criteria and a few rare elements, the screened dataset spans nearly the entire periodic table, reflecting the unbiased nature of our selection process. The shift current response tensor σ^{abc} is a third-order tensor with 18 independent components. Considering the structural symmetry of crystal, σ^{abc} may be further simplified. Fig. 3(a) displays the maximum values of the shift current response tensor at the PBE level for 2,519 screened materials, along with their distributions relative to the photon energy and the band gap. Our work identified 32 candidate materials under the condition that the absolute value of the shift current tensor element exceed $100 \mu\text{A}/\text{V}^2$. The colorbar on the right in the Fig. 3(a) shows the band gaps of the top 32 compounds with $|\sigma^{abc}|_{\text{max}} > 100 \mu\text{A}/\text{V}^2$, and gray circles indicate the remaining screened materials. It can be found that the maximum shift current tensor $|\sigma^{abc}|_{\text{max}}$ spans widely from 0 to $1000 \mu\text{A}/\text{V}^2$, mainly clustering below $200 \mu\text{A}/\text{V}^2$, with corresponding photon energy ranging from 0 to 10 eV. The background color in the Fig. 3 reveals that the photon energy of the maximum shift current response falls within the IR, VIS, or UV wavelength ranges for all screened materials. Among these highly responsive materials, 20 compounds exhibit maximum shift current response peaks in the IR region, 10 in the VIS region, and 2 in the UV region. In contrast, previously reported materials predominantly displayed shift current response in the VIS or UV wavelength ranges. More importantly, the compounds with the strongest response include $\text{Sn}_5\text{Ge}_2(\text{SbTe}_5)_2$ (mp-1219067), $\text{Ge}(\text{SbTe}_2)_2$ (mp-1224350), BiSb (mp-1227290), $\text{Bi}_2\text{Te}_4\text{Pb}$ (mp-1227398), and $\text{SnGe}_4\text{Te}_4\text{Se}$ (mp-1218953), all of which exhibit shift current response in the IR region, with peak intensities exceeding $400 \mu\text{A}/\text{V}^2$. In particular, $\text{Sn}_5\text{Ge}_2(\text{SbTe}_5)_2$ (mp-1219067) even presents a giant shift current response, with peak intensities reaching as high as $1000 \mu\text{A}/\text{V}^2$ at the PBE level.

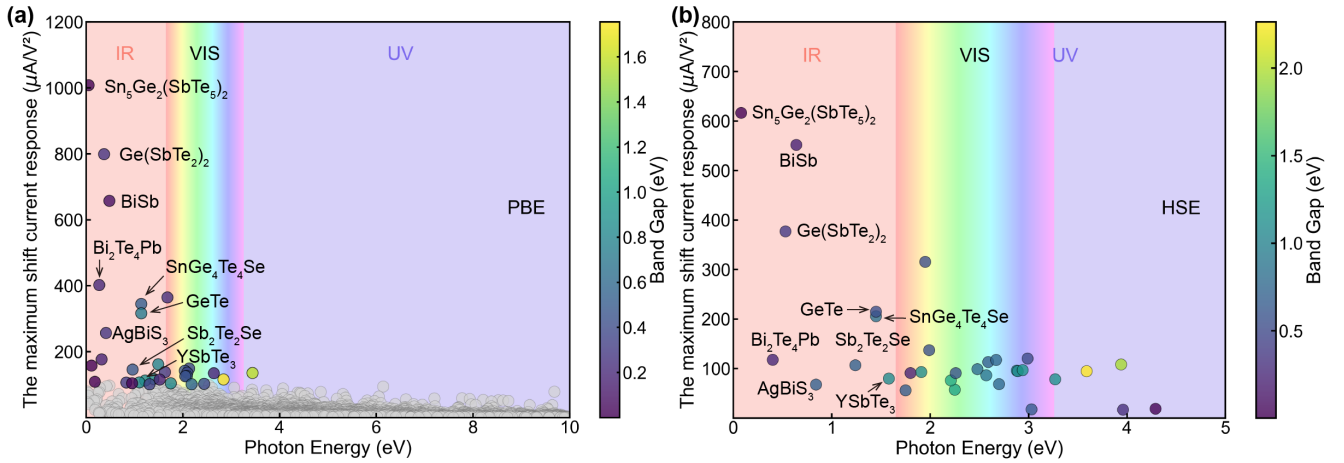


Figure 3. The calculated maximum shift current response tensor and its corresponding photon energy at the (a) PBE and (b) HSE levels, with the colorbar revealing the band gap of 32 compounds with shift current conductivity of over $100 \mu\text{A}/\text{V}^2$ and the gray circles indicate the remaining compounds. The background color reveals the response wavelength of the calculated materials, which falls within the infrared (IR), visible (VIS), or ultraviolet (UV) spectrum. The 9 compounds in Tab. 1 that exhibit IR shift current response are labeled.

For the top 32 candidates with large shift current, there are 30 bulk materials and 2 two-dimensional materials, covering a wide range of compounds from binary to pentanary compounds. The most preferred combination of elements is Bi-Se-Te, which appears three times in 32 compounds. Next are the combinations of Ge-Sb-Te, Ge-Se-Sn-Te, Ge-Li-Sb-Te, and Sb-Se-Te, each of which appears twice in 32 compounds. Obviously, the element Te has strong superiority in the enhancement of shift current. The periodic table in the inset of Fig. 4 shows the elemental distribution of these 32 compounds, and the blue numbers below the chemical symbols represent the number of occurrences of each element in different materials. The results illustrate the superiority of Te, Sb, Ge, and Se elements in enhancing shift current response. This aligns with previous studies that have reported significant BPVE in tellurium films³⁴. In addition, Qian et al.³⁵ also discovered that elemental two-dimensional ferroelectrics (As, Sb, Bi) exhibit strong shift current response in the VIS range using first-principles calculations. The pie chart in the inset of Fig. 4 reveals that these 32 compounds contain a total of eight point group symmetries, with the C_{3v} point

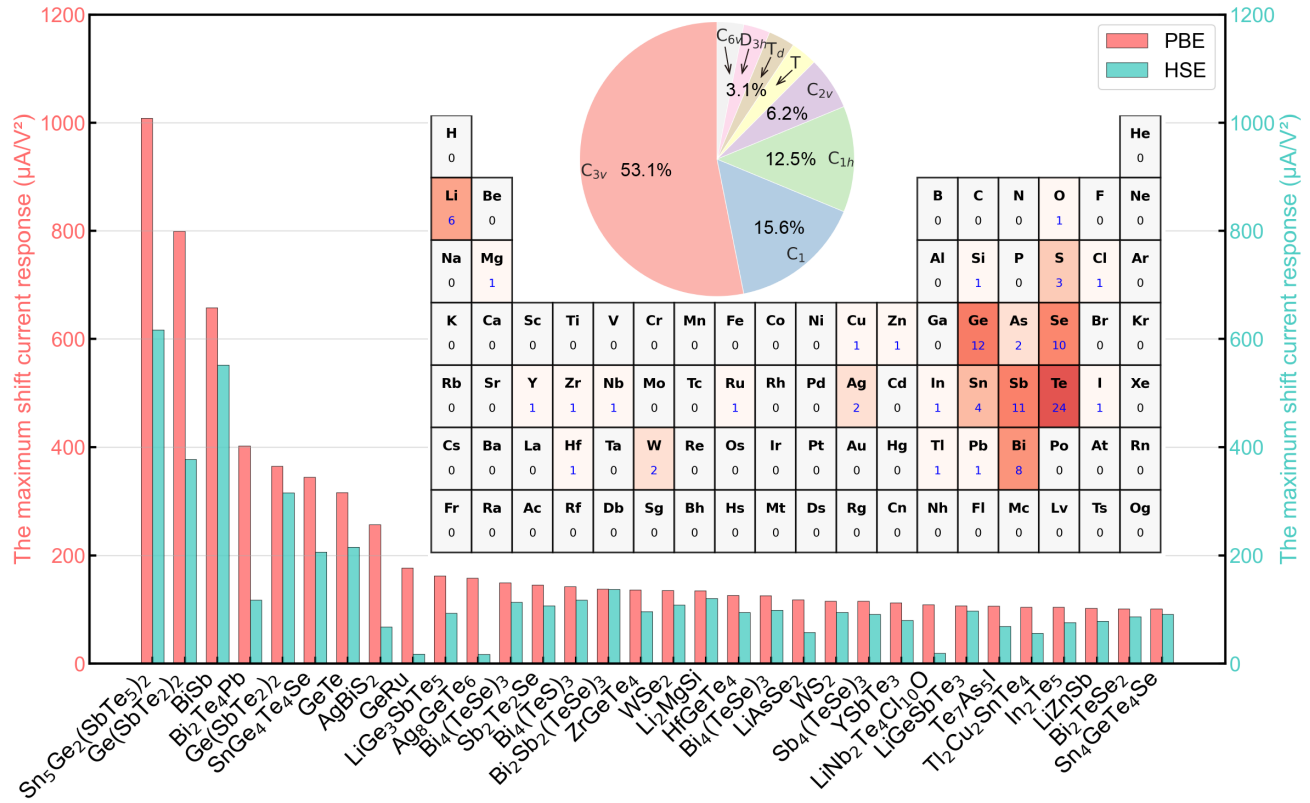


Figure 4. The calculated the maximum peak of the shift current at the PBE and HSE levels for 32 compounds with higher nonlinear optical response. The pie chart in the inset displays the relative proportions of 8 noncentrosymmetric point groups among these 32 compounds, while the periodic table on the right illustrates their elemental distribution and frequencies.

group accounting for 53.1% and the C_1 and C_{1h} point groups also accounting for a significant proportion. In particular, the top seven compounds with the largest shift current all crystallize in the trigonal $R\bar{3}m$ space group (No. 160), belonging to the C_{3v} symmetry point. Based on the above analysis, we can conclude that the PBE screening successfully identifies a key design principle: materials with the C_{3v} point group and containing Te, Sb, Ge, and Se elements are more favorable for generating stronger shift current response.

Undoubtedly, the DFT calculation of the PBE level serves as an effective screening tool to identify promising candidate materials. With possible underestimation of bandgaps, we conducted further calculations using the more accurate HSE method. Fig. 3(b) displays the maximum values of the shift current response tensor at the HSE level for top 32 candidates, along with their distributions relative to the photon energy and the band gap. The histograms in Fig. 4 provide a more intuitive comparison of the PBE and HSE results for the maximum shift current response across the top 32 compounds. As expected, the largest shift current response, calculated at the HSE level, shows a distinct reduction. For example, the maximum shift current conductivity decreased by about 39% for Sn₅Ge₂(SbTe₅)₂ (mp-1219067) (from 1008 to 616 $\mu A/V^2$), by about 53% for Ge(SbTe₂)₂ (mp-1224350) (from 799 to 377 $\mu A/V^2$), and by about 16% for BiSb (mp-1227290) (from 657 to 552 $\mu A/V^2$). Even more pronounced is the reduction in Bi₂Te₄Pb (mp-1227398), which decreased from 402 to 118 $\mu A/V^2$ ($\sim 71\%$), AgBiS₂ (mp-675977), which decreased from 257 to 68 $\mu A/V^2$ ($\sim 73\%$), GeRu (mp-1025397), which decreased from 177 to 18 $\mu A/V^2$ ($\sim 90\%$), and LiNb₂Te₄Cl₁₀O (mp-1235095), which decreased from 109 to 19 $\mu A/V^2$ ($\sim 82\%$). The detailed comparison of results is presented in Supplementary Tab. 1. In addition to lower NLO response peaks, due to the correction of the band gap by the HSE hybrid functional, the photon energy corresponding to the maximum shift current response of most systems shifts toward higher energies, causing some compounds that were originally in the IR wavelength range to move to the VIS wavelength range (as shown in Fig. 3(b)). Specifically, among the top 32 candidate materials, 9 compounds have a shift current response in the IR region, 18 in the VIS region, and 5 in the UV region.

Candidates working in the IR frequencies

Based on high-throughput PBE and HSE calculations, we identified 9 materials exhibiting strong IR shift current response (Tab. 1). $\text{Sn}_5\text{Ge}_2(\text{SbTe}_5)_2$ (mp-1219067) is predicted to be metallic, while the remaining eight are narrow-gap semiconductors with bandgaps of 0.21–1.09 eV. With the exception of AgBiS_2 (mp-675977), all compounds crystallize in the layered trigonal $R\bar{3}m$ structures with C_{3v} symmetry and broken inversion symmetry. Further symmetry analysis reveals distinct tensor properties for these materials. C_{3v} materials exhibit four independent, non-vanishing components of the shift current response: $xyx = yxx = -yyy$, $xxz = yyz$, $zxx = zyy$ and zzz . In contrast, AgBiS_2 (with C_{1h} symmetry) shows ten non-vanishing components: xxx , xxz , xyy , xzz , yxy , yyz , zxx , zxz , zyy and zzz . For all C_{3v} compounds, the in-plane xyx (yxx/yyy) component dominates the shift current response, with maximum values presented in Tab. 1 (HSE results, with PBE values in parentheses). In contrast, for AgBiS_2 , PBE calculations predict a strong xxx peak of $257 \mu\text{A}/\text{V}^2$, which disappears at the HSE level. Instead, a new xyy peak of approximately $68 \mu\text{A}/\text{V}^2$ emerges near 0.84 eV, as shown in Fig. 6(i). Among the 9 IR-active materials, BiSb (mp-1227290), GeTe (mp-938), and $\text{SnGe}_4\text{Te}_4\text{Se}$ (mp-1218953) are thermodynamically stable, while the remaining six are metastable. Our screening successfully reproduces the shift current effect in BiSb and GeTe , consistent with prior work by Yang et al. on pressure and symmetry modulation in BiSb ³⁶ and Tiwari et al. on enhanced response in monolayer GeTe ³⁷.

Table 1. The screened candidates at the HSE level exhibiting significant shift current response in the IR regions. E_{hull} represents the energy above the convex hull. E_g represents the calculated bandgap value. $|\sigma^{abc}|_{\text{max}}$ is the peak value of the maximum component in the shift current spectra. E_{photon} is the photon energy corresponding to the maximum response peak. Component reveals the maximum shift current tensor element. The values or components in parentheses are the results of PBE calculations.

Material_id	Formula	Point group	E_{Hull} (meV)	E_{gap} (eV)	$ \sigma^{abc} _{\text{max}}$ ($\mu\text{A}/\text{V}^2$)	E_{photon} (eV)	Component
mp-1219067	$\text{Sn}_5\text{Ge}_2(\text{SbTe}_5)_2$	C_{3v}	29	0.00 (0.00)	616 (1008)	0.08 (0.05)	$xyx = yxx = -yyy$
mp-1227290	BiSb	C_{3v}	0	0.21 (0.06)	552 (657)	0.64 (0.48)	$xyx = yxx = -yyy$
mp-1224350	$\text{Ge}(\text{SbTe}_2)_2$	C_{3v}	17	0.38 (0.26)	377 (799)	0.53 (0.37)	$xyx = yxx = -yyy$
mp-938	GeTe	C_{3v}	0	0.99 (0.72)	215 (316)	1.45 (1.14)	$xyx = yxx = -yyy$
mp-1218953	$\text{SnGe}_4\text{Te}_4\text{Se}$	C_{3v}	0	0.85 (0.52)	206 (345)	1.45 (1.14)	$xyx = yxx = -yyy$
mp-1227398	$\text{Bi}_2\text{Te}_4\text{Pb}$	C_{3v}	27	0.25 (0.19)	118 (402)	0.40 (0.27)	$xyx = yxx = -yyy$
mp-1219475	$\text{Sb}_2\text{Te}_2\text{Se}$	C_{3v}	32	0.70 (0.48)	107 (146)	1.24 (0.96)	$xyx = yxx = -yyy$
mp-1215924	YSbTe_3	C_{3v}	32	1.09 (0.87)	80 (112)	1.58 (1.22)	$xyx = yxx = -yyy$
mp-675977	AgBiS_2	C_{1h}	47	0.69 (0.27)	68 (257)	0.84 (0.41)	xyy (xxx)

The electronic band structures of 9 infrared NLO candidates and their corresponding shift current spectra are depicted in Fig. 5 and Fig. 6, respectively. The element-resolved and orbital-projected electronic density of states (DOS) at the HSE level are displayed in Supplementary Fig. 1–3. From the perspective of the photon energy corresponding to the maximum shift current response, four compounds exhibit MIR response, while five show near-infrared (NIR) response.

The most striking candidates is $\text{Sn}_5\text{Ge}_2(\text{SbTe}_5)_2$ (mp-1219067), which crystallizes in layered Te-Sb-Te-Sb-Te-Ge-Te-Ge-Te-Sn-Te-Sn-Te-Sn-Te-Sn-Te-Sn-Te-Sn-Te sheets along the (0 0 1) direction. Despite the MP database claiming that it has a band gap of 0.19 eV, our calculation of electronic structure at both PBE and HSE levels reveal metallic behavior without a direct gap, as shown in Fig. 5(a). Nevertheless, small indirect gaps of ~ 0.04 eV persist near the Γ and Z high-symmetry points, expanding to ~ 0.1 eV along the Γ -L and Z-L paths. The electronic DOS in Supplementary Fig. 1(a) and Supplementary Fig. 2(a) reveals that the valence band of $\text{Sn}_5\text{Ge}_2(\text{SbTe}_5)_2$ (mp-1219067) is dominated by Te- p states, while the conduction band is primarily formed by Sb- p and Ge- p orbitals. This delocalized p -orbital character near the Fermi level is consistent with previously reported trends favoring enhanced shift current response³⁸. Fig. 6(a) illustrates the shift current spectra at both PBE and HSE levels for $\text{Sn}_5\text{Ge}_2(\text{SbTe}_5)_2$ (mp-1219067). In the MIR range, $\text{Sn}_5\text{Ge}_2(\text{SbTe}_5)_2$ (mp-1219067) exhibits pronounced peaks across multiple tensor components: the xyx (yxx/yyy) component reaches $616 \mu\text{A}/\text{V}^2$ at 0.08 eV, while the xxz (yyz) and zxx (zyy) attain $361 \mu\text{A}/\text{V}^2$ and $480 \mu\text{A}/\text{V}^2$ at 0.14 eV and 0.12 eV, respectively (at the HSE level). These strong responses in the MIR range originate primarily from robust electron transitions between the valence band and the conduction band. PBE systematically overestimates these magnitudes, as mentioned earlier. Furthermore, $\text{Sn}_5\text{Ge}_2(\text{SbTe}_5)_2$ (mp-1219067) shows a

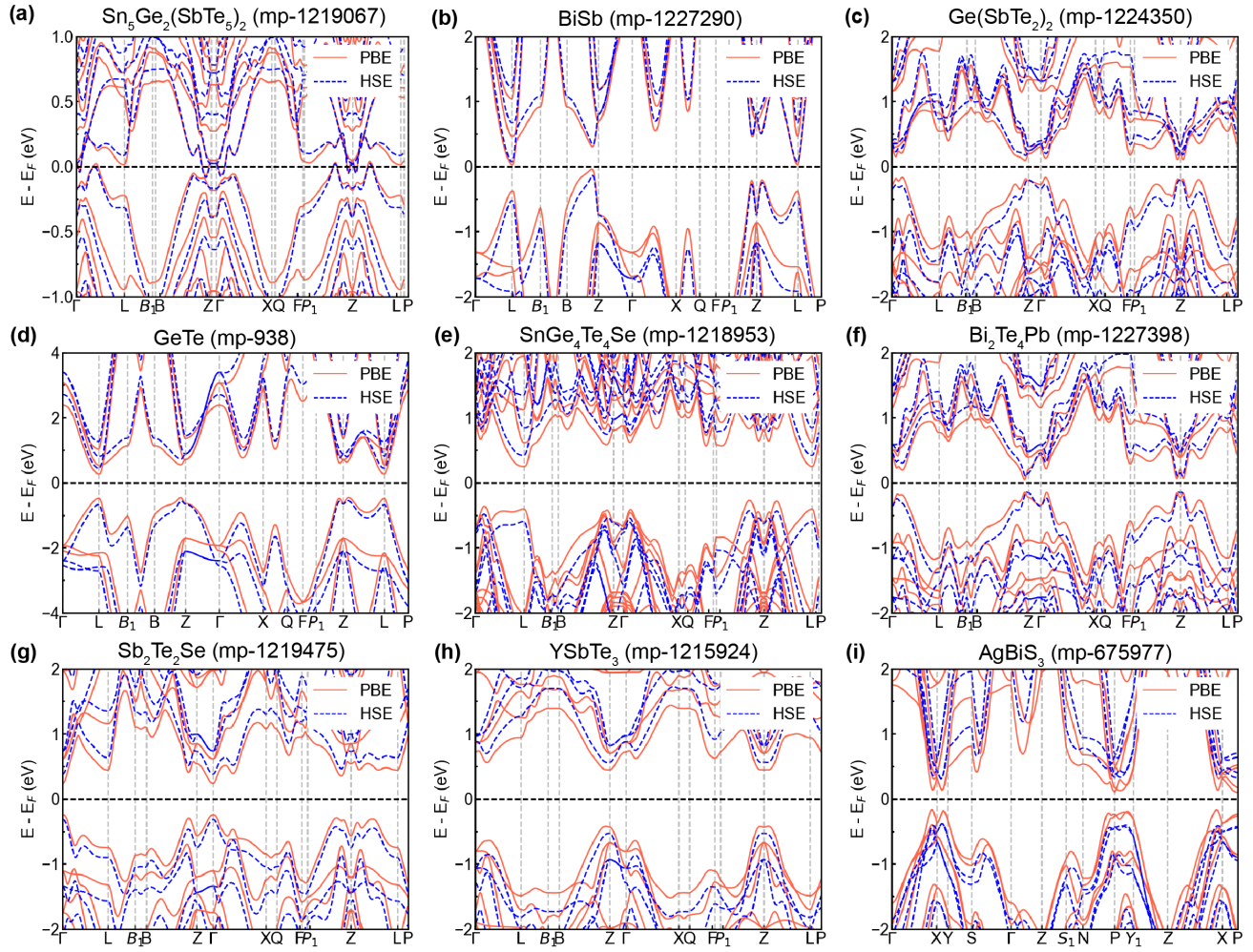


Figure 5. The Band structures for the infrared candidates. Red solid lines and blue dashed lines correspond to PBE and HSE results, respectively.

strong visible-light response, with the xxz (yyz) component exceeding $500 \mu A/V^2$ across the 1.7–2.4 eV range.

BiSb (mp-1227290) adopts a layered hexagonal structure composed of alternating Sb and Bi atomic bilayers stacked along the c axis with weak vdW interlayer bonding. Electronic structure calculations at both PBE and HSE levels (Fig. 5(b)) confirm it as an indirect-gap semiconductor with a 0.2 eV bandgap at the HSE level, consistent with previous reports^{36,39}. The valence band maximum lies along the B-Z direction, while the conduction band minimum is located near the L point, corresponding to direct gaps of 0.48 eV and 0.6 eV, respectively. The electronic DOS (Supplementary Fig. 1(b) and Supplementary Fig. 2(b)) reveals that the valence band is dominated by Sb- p states with minor Bi contribution, whereas the conduction band features primarily Bi- p character. This delocalized p -orbital contribution near the Fermi level enhances the shift current response. The calculated shift current spectra (Fig. 6(b)) reflect these electronic features: HSE corrections reduce the σ^{xxz} , σ^{zxx} , and σ^{zzz} peaks from 609, 478, and $158 \mu A/V^2$ (PBE) to 362, 235, and $56 \mu A/V^2$, respectively, while blue-shifting their photon energies from 0.47, 0.50, and 0.51 eV to 0.65, 0.72, and 0.78 eV. In contrast, the in-plane σ^{yyy} peak shows greater resilience, decreasing only modestly from 657 to $552 \mu A/V^2$ with a blue-shift from 0.48 to 0.64 eV. This confirms that the shift current response for BiSb (mp-1227290) lies entirely within the IR spectral range.

Ge(SbTe₂)₂ (mp-1224350) and Bi₂Te₄Pb (mp-1227398) share similar seven-layer crystal structures stacked along the z -direction of the hexagonal unit cell in the sequence Te-Ge/Pb-Te-Sb/Bi-Te-Sb/Bi-Te sequence. Fig. 5(c) and 5(f) display respectively the band structures of Ge(SbTe₂)₂ (mp-1224350) and Bi₂Te₄Pb (mp-1227398), with band gaps of 0.38 eV and 0.25 eV, at the HSE level. The electronic DOS in Supplementary Fig. 1(c, f) and Supplementary Fig. 2(c, d) reveal that Te- p states dominate the valence bands of both compounds, while their conduction bands are primarily formed by Sb- p (Ge(SbTe₂)₂) and Bi- p (Bi₂Te₄Pb) orbitals. Consequently, Bi₂Te₄Pb exhibits a lower IR shift current peak than Ge(SbTe₂)₂ (Figs. 6(c) and

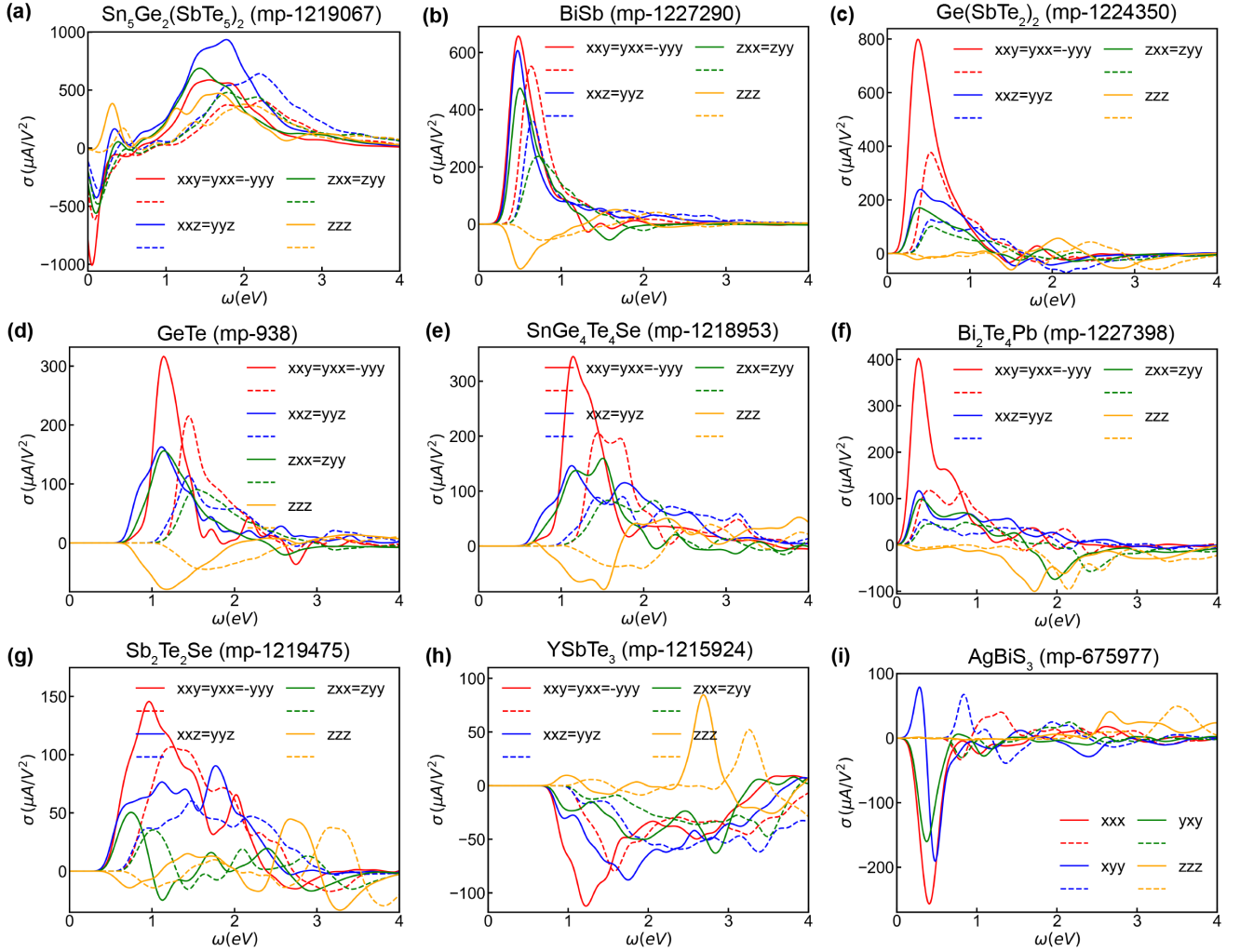


Figure 6. The shift current response spectra for the infrared candidates. Solid lines and dashed lines correspond to PBE and HSE results, respectively.

6(f)), likely due to its reduced band edge density of states.

GeTe (mp-938), SnGe₄Te₄Se (mp-1218953), Sb₂Te₂Se (mp-1219475), and YSbTe₃ (mp-1215924) are layered compounds with larger bandgaps than the MIR materials, enabling shift current response at higher energies. Their electronic band structures are shown in Fig. 5(d-h), while the corresponding shift current spectra in Fig. 6(d-h) reveal strong shift current responses across a broad range from the NIR to the VIS spectrum.

Overall, through high-throughput first principles calculations, we identified 9 IR shift current materials, seven of which were newly discovered. The strongest shift current response reaches 616 $\mu\text{A}/\text{V}^2$, which is four times greater than that of the previously reported IR-responsive topological semimetal TaAs²¹. These discoveries establish a rich platform for IR detection, imaging, and energy conversion. Our work significantly expands the shift current material database into the IR spectral range, laying a theoretical foundation for subsequent experimental verification and device design.

Application of the dataset for AI-driven screening

The comprehensive dataset generated by our high-throughput screening serves as a foundational resource for data-driven discovery. As a demonstration, we utilized the DeepMD-kit⁴⁰ to train our DFT database for the coarse screening of potential candidates with strong shift current response from the large-scale MP database, thereby narrowing the scope for subsequent precise calculations. Instead of training a model from scratch, we adopted a transfer learning strategy based on the DPA3 graph neural network (GNN)⁴¹, a pre-trained large atomic model originally designed for interatomic potentials. We refer to this specialized shift-current predictor as **DPA3- σ** . Specifically, DPA3- σ utilizes the pre-trained DPA3 parameters to generate high-quality structural embeddings, which are then mapped to the maximum shift current response $\sigma = |\sigma^{abc}(\omega)|_{\max}$ via a

multi-layer perceptron (MLP) (Fig. 7(a)). The DFT dataset (structures with $N_{atom} < 20$) was randomly split into training (80%) and validation (20%) sets. By leveraging the geometric features encoded in the pre-trained DPA3, DPA3- σ significantly improves prediction efficiency on our finite dataset. We also applied a log-transformation $y = \ln(1 + \sigma)$ to the target variable to mitigate the impact of large numerical variations.

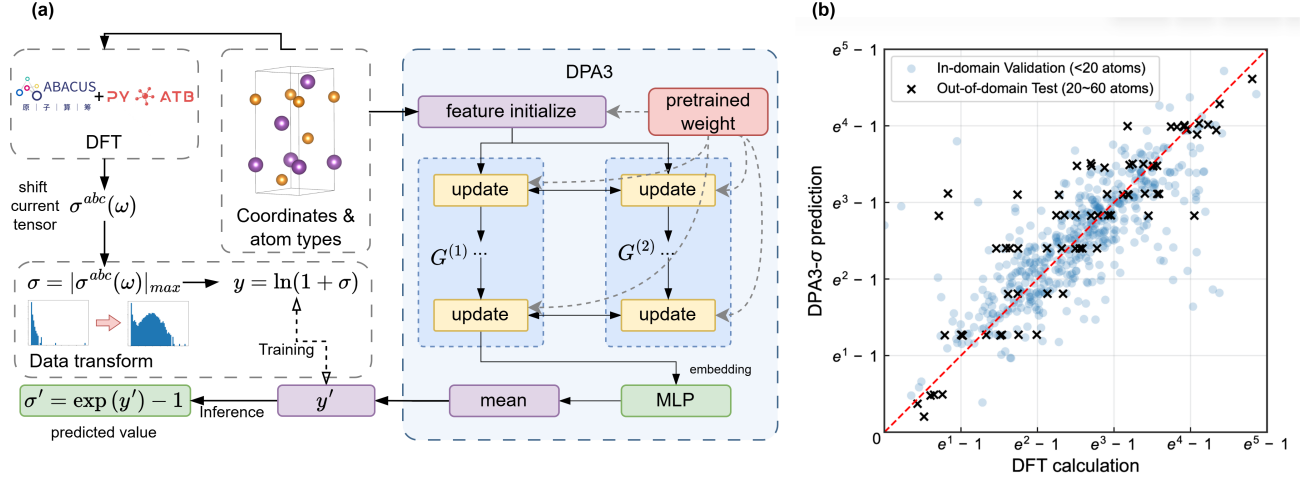


Figure 7. Architecture and performance of the DPA3- σ model. (a) Schematic illustration of the training pipeline. The workflow integrates high-throughput DFT data generation with a transfer learning strategy, where the DPA3 backbone is initialized with pre-trained weights to extract geometric features. These features are mapped to the log-transformed maximum shift current via a Multi-Layer Perceptron (MLP). (b) Parity plot comparing DPA3- σ predictions with DFT-calculated values. The plot distinguishes between the in-domain validation set (blue dots, < 20 atoms) and the out-of-domain test set (black crosses, $20-60$ atoms), demonstrating the model’s generalizability to larger unseen systems. The red dashed line indicates perfect agreement.

Table 2. Comprehensive performance evaluation of the DPA3- σ model on the in-domain ($N = 498$) and out-of-domain set ($N = 73$). The upper table details the regression metrics in the logarithmic domain ($y = \ln(1 + \sigma)$), categorized by the magnitude of the DFT-calculated shift current. The lower table evaluates the model’s utility as a binary screener using a threshold of 0.8 times the target values ($\sigma > 100 \mu A/V^2$ and $\sigma > 80 \mu A/V^2$). The high recall rate highlights the model’s effectiveness in identifying top-tier candidates.

Regression Metrics (Target: $y = \ln(1 + \sigma)$)				
Category	Small	Medium	Large	Overall
Range ($\sigma, \mu A/V^2$)	(0, 50]	(50, 100]	(100, ∞)	All
Mean DFT (y)	2.43	4.14	5.44	2.56
Mean Pred. (y')	2.46	3.46	4.47	2.54
MAE (\downarrow)	0.34	0.72	0.97	0.37
MAPE (\downarrow) (%)	19.33	17.30	17.00	19.18
Screening Performance (Threshold: Target $\times 0.8$)				
Target	Recall	Precision	Accuracy	F1-Score
$\sigma > 100 \mu A/V^2$	80.0%	80.0%	99.6%	80.0%
$\sigma > 80 \mu A/V^2$	85.7%	60.0%	99.1%	70.6%

To rigorously assess the generalizability of DPA3- σ beyond the training domain, we evaluated its performance on a combined dataset consisting of an **in-domain validation set** ($N = 498$, < 20 atoms) and an **out-of-domain test set** ($N = 73$,

20 – 60 atoms). As illustrated in Fig. 7(b), the model demonstrates high fidelity for in-domain structures (blue dots) and, crucially, maintains strong predictive correlation for larger, out-of-domain systems (black crosses). This confirms that the model has learned transferable geometric features rather than merely overfitting to small systems. Quantitative regression analysis (Table 2, upper panel) further supports this observation. To assess the prediction accuracy in the logarithmic domain, we utilized the Mean Absolute Error (MAE) and Mean Absolute Percentage Error (MAPE), defined as:

$$\text{MAE} = \frac{1}{n} \sum_{i=1}^n |y_i - y'_i|, \quad \text{MAPE} = \frac{1}{n} \sum_{i=1}^n \left| \frac{y_i - y'_i}{y_i} \right| \times 100\%.$$

where y_i and y'_i denote the DFT-calculated and predicted values, respectively. Using these metrics, we find that the model effectively differentiates response magnitudes across the diverse test set: the predicted mean for the 'Large' group (4.47) is clearly distinct from the 'Small' group (2.46). This significant separation ($\Delta \approx 2.0$), which far exceeds the overall MAE (0.37), validates the model's robust discriminative power for screening purposes.

To translate these predictive capabilities into a practical screening workflow, we evaluated the utility of DPA3- σ as a binary classifier (Table 2, lower panel). Given the model's tendency to slightly underestimate peak values (conservative prediction), we implemented a systematic "safety margin" strategy by setting the model's screening threshold to 0.8 times the desired target value (Threshold = $0.8 \times \text{Target}$). We validated this strategy against two distinct targets. First, for our primary goal of identifying candidates with DFT-calculated responses $\sigma > 100 \mu\text{A}/\text{V}^2$, we set the model threshold to $80 \mu\text{A}/\text{V}^2$. This approach yielded an impressive Recall of 80.0%, meaning it successfully retrieved 4 out of 5 true high-performance candidates, and a Precision of 80.0%, indicating a high "hit rate" that minimizes wasted calculations on false positives. Second, to assess robustness on a broader set of candidates, we targeted materials with responses $\sigma > 80 \mu\text{A}/\text{V}^2$, which achieved an even higher Recall of 85.7%. These consistent results confirm that the DPA3- σ can reliably retrieve the vast majority of high-performance materials while maintaining high efficiency.

Finally, to demonstrate the practical value of this AI-driven workflow, we applied DPA3- σ to screen the remaining 6,008 non-centrosymmetric materials in the MP database (Supplementary Fig. 4). We specifically targeted complex systems with more than 30 atoms—a regime computationally expensive for exhaustive DFT screening. From the top predictions, we selected 10 candidates for validation, successfully identifying two new large-cell materials, $\text{Cs}(\text{Bi}_2\text{Te}_3)_2$ (mp-672338) and $\text{Sn}(\text{BiTe}_2)_2$ (mp-677596), with confirmable high responses (Supplementary Tab. 2). Remarkably, this successful discovery using a simplified scalar target ($|\sigma^{abc}|_{\text{max}}$) serves as a compelling proof-of-concept, demonstrating that our high-quality dataset enables effective AI-driven material design even with straightforward modeling strategies.

Discussion

In summary, we screened 2,519 candidate materials with broken inversion symmetry by applying a multi-step filter to the the MP database, evaluating their shift current responses using high-throughput DFT calculations. Ultimately, 32 NLO materials with significant shift current responses ($\sigma > 100 \mu\text{A}/\text{V}^2$) were identified, including 9 compounds that are active in the IR region. In particular, $\text{Sn}_5\text{Ge}_2(\text{SbTe}_5)_2$ (mp-1219067) stands out with an exceptional shift current response of $616 \mu\text{A}/\text{V}^2$, which is four times greater than that of the previously reported topological semimetal TaAs²¹. Most of these materials possess layered structures with C_{3v} symmetry and heavy p -block elements (e.g. Te, Sb), featuring narrow bandgaps, strong NLO response, and favorable thermodynamic stability. They hold broad application prospects in infrared photodetection, bias-free self-driven sensing, broadband energy harvesting, and deep biomedical modulation. Our work bridges a critical gap in NLO material screening, successfully extending the shift current operational window from the VIS/UV into the IR spectral region.

Beyond significantly enhancing the efficiency and scope of materials discovery, high-throughput calculations establish comprehensive, high-quality datasets that underpin data-driven material design and machine learning. As a demonstration, we validated the feasibility of DPA3- σ -based methods for preliminary database screening. Moreover, our first-principles shift current tensor dataset opens extensive avenues for future exploration, including identifying optimal descriptors beyond simple maxima, predicting complete frequency-dependent tensors, and expanding beyond the MP database. Overall, this work establishes a critical foundation for AI-driven accelerated discovery of high-performance NLO materials.

Methods

Theory of the shift current response

The shift current constitutes an essential mechanism underlying the BPVE in non-centrosymmetric materials⁴². It describes the photocurrent generated by light illumination on homogeneous crystals without inversion symmetry. As a second-order NLO response, the shift current can be expressed as a direct current induced by a monochromatic light excitation with the form of $\mathbf{E}(t) = \mathbf{E}(\omega)e^{i\omega t} + \mathbf{E}(-\omega)e^{-i\omega t}$, where

$$J_{\text{shift}}^a = 2\sigma^{abc}(0; \omega, -\omega)E^b(\omega)E^c(-\omega) \quad (1)$$

where a, b, c are Cartesian indices, with a specifying the current direction and b and c incident light polarization. The shift current conductivity σ^{abc} is given by

$$\sigma^{abc}(0; \omega, -\omega) = -\frac{i\pi e^3}{2\hbar^2} \int \frac{dk}{(2\pi)^3} \sum_{n,m} f_{nm} (I_{nm}^{abc} + I_{mn}^{acb}) \times \delta(\omega_{nm} - \omega) \quad (2)$$

where $\hbar\omega_{nm} = E_n - E_m$ represents photon energy, $f_{nm} = f(E_n) - f(E_m)$ is the Fermi-Dirac occupation number. The integrand I_{nm}^{abc} can be written out with Berry connections and derivatives of Berry connections

$$I_{nm}^{abc} = r_{mn}^b r_{nm;a}^c \quad (3)$$

where r_{nm}^b and $r_{nm;a}^b$ are given by

$$r_{nm}^b = (1 - \delta_{nm}) A_{nm}^b \quad (4)$$

and

$$r_{nm;a}^b = \partial_{k_a} r_{nm}^b - i(A_{nn}^a - A_{mm}^a) r_{nm}^b \quad (5)$$

respectively, here the Berry connection is defined as

$$A_{nm}^b \equiv i \langle u_n | \partial_b u_m \rangle \quad (6)$$

where $|u_m\rangle$ denotes the periodic part of a Bloch eigenstate. Since a δ function is present in the expression of σ^{abc} , a very fine k mesh is needed to achieve convergence.

Under linearly polarized light ($b = c$), equation (2) can be reformulated into a more transparent form

$$\sigma^{abb}(0; \omega, -\omega) = \frac{\pi e^3}{\hbar^2} \int [dk] \sum_{n,m} f_{nm} R_{nm}^{a,b} \times r_{nm}^b r_{mn}^b \times \delta(\omega_{nm} - \omega), \quad (7)$$

where $R_{nm}^{a,b}$ is shift vector defined as

$$R_{nm}^{a,b} = \partial_{k_a} \phi_{nm}^b - A_{mm}^a + A_{nn}^a \quad (8)$$

and ϕ_{nm}^b is the phase of $r_{nm}^b = |r_{nm}^b| e^{-i\phi_{nm}^b}$. $R_{nm}^{a,b}$ has a unit of length and can be physically interpreted as the average displacement of the coherent photoexcited carriers during their lifetimes. The product $r_{nm}^b r_{mn}^b \delta(\omega_{nm} - \omega)$ can be interpreted as the transition rate from band m to band n according to the Fermi golden rule. That is, shift current tensor can be expressed as transition rate from band m to band n multiplied by shift vector between the two bands.

DFT calculation details

We started with the structures provided by the MP database and performed first-principles DFT calculations based on the numerical atomic bases (NAOs), which is more suitable for calculations of large systems⁴³. The DFT Hamiltonian and band structures were obtained using the first-principles software package ABACUS^{44,45}. The charge density converges to within 1×10^{-8} e/a.u.³ and the k -point mesh with a spacing of $0.03 \text{ } 2\pi/\text{\AA}$ for self-consistent field (SCF) calculations. In ABACUS, we employed double-zeta polarized (DZP) pseudo-atomic orbitals basis set to balance computational accuracy and efficiency. The SG15 optimized Norm-Conserving Vanderbilt (ONCV) multi-projector pseudopotentials⁴⁶ and the atomic basis⁴⁷ paired with the SG15 pseudopotential are used. We verified that our basis sets for high-throughput calculations yield similar band structures to those provided by the MP database. We adopted the PBE form of the exchange-correlation functional³⁰ for the filtered 2,519 materials and the Heyd-Scuseria-Ernzerhof 2006 (HSE06) screened hybrid functional^{31,32} for the top 32 candidates, which generally yields more accurate electronic band gaps than PBE. For the out-of-domain test set with over 20 atoms, the PBE functional³⁰ was used for first-principles evaluation.

Optical responses, such as the second-order shift current tensor σ , are calculated using the Python Ab-initio Tight-Binding (PYATB) package¹⁴ based on the DFT Hamiltonian obtained from ABACUS. Our tests show that the k -point mesh spacing of $0.02 \text{ } 2\pi/\text{\AA}$ is sufficient for the convergence of frequency-dependent shift-current responses in most cases, while we also noticed that a denser k -mesh is necessary for few cases.

References

1. Krishna, S. Quantum dots-in-a-well infrared photodetectors. *J. Phys. D: Appl. Phys.* **38**, 2142 (2005).
2. Brongersma, M. L., Halas, N. J. & Nordlander, P. Plasmon-induced hot carrier science and technology. *Nat. Nanotechnol.* **10**, 25–34 (2015).
3. Chapin, D. M., Fuller, C. S. & Pearson, G. L. A new silicon p-n junction photocell for converting solar radiation into electrical power. *J. Appl. Phys.* **25**, 676–677 (1954).
4. Funahashi, M. High open-circuit voltage under the bulk photovoltaic effect for the chiral smectic crystal phase of a double chiral ferroelectric liquid crystal doped with a fullerene derivative. *Mater. Chem. Front.* **5**, 8265–8274 (2021).
5. Shockley, W. & Queisser, H. J. Detailed balance limit of efficiency of p-n junction solar cells. *J. Appl. Phys.* **32**, 510–519 (1961).
6. Spanier, J. E. *et al.* Power conversion efficiency exceeding the Shockley–Queisser limit in a ferroelectric insulator. *Nat. Photonics* **10**, 611–616 (2016).
7. Fridkin, V. M. Bulk photovoltaic effect in noncentrosymmetric crystals. *Crystallogr. Reports* **46**, 654–658 (2001).
8. Dang, Y. & Tao, X. Recent progress of bulk photovoltaic effect in acentric single crystals and optoelectronic devices. *Matter* **5**, 2659–2684 (2022).
9. Dai, Z. & Rappe, A. M. Recent progress in the theory of bulk photovoltaic effect. *Chem. Phys. Rev.* **4**, 011303 (2023).
10. Dai, Z., Schankler, A. M., Gao, L., Tan, L. Z. & Rappe, A. M. Phonon-assisted ballistic current from first-principles calculations. *Phys. Rev. Lett.* **126**, 177403 (2021).
11. Dai, Z. & Rappe, A. M. First-principles calculation of ballistic current from electron-hole interaction. *Phys. Rev. B* **104**, 235203 (2021).
12. Tiwari, R. P., Birajdar, B. & Ghosh, R. K. First-principles calculation of shift current bulk photovoltaic effect in two-dimensional α -In₂Se₃. *Phys. Rev. B* **101**, 235448 (2020).
13. Ibañez Azpiroz, J., Tsirkin, S. S. & Souza, I. Ab initio calculation of the shift photocurrent by wannier interpolation. *Phys. Rev. B* **97**, 245143 (2018).
14. Jin, G., Pang, H., Ji, Y., Dai, Z. & He, L. Pyatb: An efficient python package for electronic structure calculations using ab initio tight-binding model. *Comput. Phys. Commun.* **291**, 108844 (2023).
15. Young, S. M. & Rappe, A. M. First principles calculation of the shift current photovoltaic effect in ferroelectrics. *Phys. Rev. Lett.* **109**, 116601 (2012).
16. Cook, A. M., Fregoso, B. M., Juan, F. d., Coh, S. & Moore, J. E. Design principles for shift current photovoltaics. *Nat. Commun.* **8**, 14176 (2017).
17. Chynoweth, A. G. Surface space-charge layers in barium titanate. *Phys. Rev.* **102**, 705–714 (1956).
18. Koch, W., Munser, R., Ruppel, W. & Würfel, P. Bulk photovoltaic effect in BaTiO₃. *Solid State Commun.* **17**, 847–850 (1975).
19. Glass, A. M., von der Linde, D. & Negran, T. J. High-voltage bulk photovoltaic effect and the photorefractive process in LiNbO₃. *Appl. Phys. Lett.* **25**, 233–235 (1974).
20. Brody, P. High voltage photovoltaic effect in barium titanate and lead titanate-lead zirconate ceramics. *J. Solid State Chem.* **12**, 193–200 (1975).
21. Osterhoudt, G. B. *et al.* Colossal mid-infrared bulk photovoltaic effect in a type-I weyl semimetal. *Nat. Mater.* **18**, 471–475 (2019).
22. Wang, Z. *et al.* Giant infrared bulk photovoltaic effect in tellurene for broad-spectrum neuromodulation. *Light. Sci. & Appl.* **13**, 277 (2024).
23. Yu, L. & Zunger, A. Identification of potential photovoltaic absorbers based on first-principles spectroscopic screening of materials. *Phys. Rev. Lett.* **108**, 068701 (2012).
24. Wang, J. *et al.* Unbiased screening of deep-ultraviolet and mid-infrared nonlinear optical crystals: Long-neglected covalent and mixed-cation motifs. *Phys. Rev. Mater.* **8**, 085202 (2024).
25. Chen, J. *et al.* Accelerating discovery of next-generation power electronics materials via high-throughput ab initio screening. *npj Comput. Mater.* **11**, 249 (2025).

26. Gorai, P., Stevanović, V. & Toberer, E. S. Computationally guided discovery of thermoelectric materials. *Nat. Rev. Mater.* **2**, 17053 (2017).
27. Li, Y. *et al.* High-throughput screening and machine learning classification of van der Waals dielectrics for 2D nanoelectronics. *Nat. Commun.* **15**, 9527 (2024).
28. Xin, J., Guo, Y. & Wang, Q. Screening two-dimensional pyroelectric materials based on pentagonal chains with large shift current. *Phys. Rev. Mater.* **7**, 074001 (2023).
29. Sauer, M. O. *et al.* Shift current photovoltaic efficiency of 2D materials. *npj Comput. Mater.* **9**, 35 (2024).
30. Perdew, J. P., Burke, K. & Ernzerhof, M. Generalized gradient approximation made simple. *Phys. Rev. Lett.* **77**, 3865–3868 (1996).
31. Heyd, J., Scuseria, G. E. & Ernzerhof, M. Hybrid functionals based on a screened Coulomb potential. *The J. Chem. Phys.* **118**, 8207–8215 (2003).
32. Lin, P., Ren, X. & He, L. Accuracy of localized resolution of the identity in periodic hybrid functional calculations with numerical atomic orbitals. *The J. Phys. Chem. Lett.* **11**, 3082–3088 (2020).
33. Jain, A. *et al.* Commentary: The Materials Project: A materials genome approach to accelerating materials innovation. *APL Mater.* **1**, 011002 (2013).
34. Cheng, M., Zhu, Z.-Z. & Guo, G.-Y. Strong bulk photovoltaic effect and second-harmonic generation in two-dimensional selenium and tellurium. *Phys. Rev. B* **103**, 245415 (2021).
35. Qian, Z., Zhou, J., Wang, H. & Liu, S. Shift current response in elemental two-dimensional ferroelectrics. *npj Comput. Mater.* **9**, 67 (2023).
36. Yang, M. & Zhang, C. Shift current engineering in BiSb. *The J. Phys. Chem. C* **128**, 13373–13378 (2024).
37. Tiwari, R. P. Enhanced shift current bulk photovoltaic effect in ferroelectric Rashba semiconductor α -GeTe: ab initio study from three- to two-dimensional van der Waals layered structures. *J. Physics: Condens. Matter* **34**, 435404 (2022).
38. Tan, L. Z. *et al.* Shift current bulk photovoltaic effect in polar materials—hybrid and oxide perovskites and beyond. *npj Comput. Mater.* **2**, 16026 (2016).
39. Singh, S., Garcia-Castro, A. C., Valencia-Jaime, I., Muñoz, F. & Romero, A. H. Prediction and control of spin polarization in a weyl semimetallic phase of BiSb. *Phys. Rev. B* **94**, 161116 (2016).
40. Wang, H., Zhang, L., Han, J. & E, W. Deepmd-kit: A deep learning package for many-body potential energy representation and molecular dynamics. *Comput. Phys. Commun.* **228**, 178–184 (2018).
41. Zhang, D. *et al.* A graph neural network for the era of large atomistic models (2025). [2506.01686](https://arxiv.org/abs/2506.01686).
42. Sipe, J. E. & Shkrebtii, A. I. Second-order optical response in semiconductors. *Phys. Rev. B* **61**, 5337–5352 (2000).
43. Li, P. *et al.* Large-scale ab initio simulations based on systematically improvable atomic basis. *Comput. Mater. Sci.* **112**, 503–517 (2016).
44. Chen, M., Guo, G.-C. & He, L. Systematically improvable optimized atomic basis sets for ab initio calculations. *J. Physics: Condens. Matter* **22**, 445501 (2010).
45. Zhou, W. *et al.* Abacus: An electronic structure analysis package for the ai era. *The J. Chem. Phys.* **163**, 192501 (2025).
46. Schlipf, M. & Gygi, F. Optimization algorithm for the generation of ONCV pseudopotentials. *Comput. Phys. Commun.* **196**, 36–44 (2015).
47. Lin, P., Ren, X. & He, L. Strategy for constructing compact numerical atomic orbital basis sets by incorporating the gradients of reference wavefunctions. *Phys. Rev. B* **103**, 235131 (2021).

Data availability

The DPA3- σ model weights are publicly available at https://huggingface.co/CLaS/DPA3-shift_current. The data supporting the findings of this study are available within the paper and its supplementary information files.

Acknowledgements

This work was supported by the National Natural Science Foundation of China (Grant No. 12125504 and No. 12504285), the National Key R&D Program of China (2022YFA1404400), and the “Hundred Talents Program” of the Chinese Academy of Sciences, and the Priority Academic Program Development (PAPD) of Jiangsu Higher Education Institutions, and the Natural Science Foundation of Jiangsu Province (BK20250472).

Author contributions statement

J.-H. Jiang initiated the study. J.-H. Jiang, Q. Gu, Q. Wang and D. Zheng co-supervised the project. A. Yang performed the high-throughput first-principles calculations. D. Jin and M. Liu performed the machine learning demonstration. A. Yang and D. Jin analyzed and visualized the results. A. Yang, D. Jin, and Q. Gu wrote the manuscript. All authors reviewed the manuscript.